Cellular Internalization of Rod-Like Nanoparticles with Various Surface Patterns: Novel Entry Pathway and Controllable Uptake Capacity

Jiaxiao Xue, Zhou Guan, Jiaping Lin, Chunhua Cai,* Wenjie Zhang, and Xinquan Jiang**

***T**he cellular internalization of rod-like nanoparticles (NPs) is investigated in a combined experimental and simulation study. These rod-like nanoparticles with smooth, abacus-like (i.e., beads-on-wires), and helical surface patterns are prepared by the cooperative self-assembly of poly(γ-benzyl-L-glutamate)-block-poly(ethylene glycol) (PBLG-b-PEG) block copolymers and PBLG homopolymers. All three types of NPs can be internalized via endocytosis. Helical NPs exhibit the best endocytic efficacy, followed by smooth NPs and abacus-like NPs. Coarse-grained molecular dynamics simulations are used to examine the endocytic efficiency of these NPs. The NPs with helical and abacus-like surfaces can be endocytosed via novel "standing up" (tip entry) and "gyroscope-like" (precession) pathways, respectively, which are distinct from the pathway of traditional NPs with smooth surfaces. This finding indicates that the cellular internalization capacity and pathways can be regulated by introducing stripe patterns (helical and abacus-like) onto the surface of rod-like NPs. The results of this study may lead to novel applications of biomaterials, such as advanced drug delivery systems.*

1. Introduction

Nanoparticles (NPs) hold significant importance for applications in biomedicine, serving as drug delivery vehicles,[1–3] imaging tools,[4,5] and gene delivery carriers,[6–8] among other functions. Among numerous fabrication methods for NPs, block copolymer self-assembly is an effective way to generate various NPs, including spheres, cylinders, and vesicles.[9–12] Micelles based on polyethylene glycol (PEG)–polypeptide amphiphilic copolymers have attracted considerable attention due to their biocompatibility and biodegradability.[2,13,14] The hydrophilicity of PEG endows the NPs with "stealth" properties, allowing them to avoid clearance by the immune system.[15] Additionally, methoxy groups at the free ends of PEG can act as nonspecific ligands.[16–18]

In most situations, NPs must be internalized into cells to perform their functions. During this process, various forces, such as van der Waals, electrostatic, solvation, solvophobic, and depletion forces, dominate the interfacial interactions between the NPs and cells.[19,20] The complicated interactions can be strongly influenced by various characteristics of NPs, including their size,[21,22] shape,[23–26] mechanical flexibility,[27,28] surface ligand,[29,30] surface charge,[19,31] and surface pattern.[32,33] In some literature reports, it was found that rod-like NPs exhibit higher delivery efficiency than their extensively studied spherical counterparts under certain conditions.[23,34,35] For instance, rod-like NPs have stronger cellular internalization capacity when the two types of NPs

J. Xue, Z. Guan, Prof. J. Lin, Dr. C. Cai
Shanghai Key Laboratory of Advanced Polymeric Materials
State Key Laboratory of Bioreactor Engineering
Key Laboratory for Ultrafine Materials of Ministry of Education
School of Materials Science and Engineering
East China University of Science and Technology
Shanghai 200237, China
E-mail: jlin@ecust.edu.cn; caichunhua@ecust.edu.cn

Dr. W. Zhang, Prof. X. Jiang
Department of Prosthodontics
School of Medicine
Ninth Hospital Affiliated to Shanghai Jiao Tong University
639 Zhizaoju Road, Shanghai 200011, China
E-mail: xinquanj@aliyun.com

DOI: 10.1002/smll.201604214

have the same volume,[23] or when the rod-like NPs possess a specific aspect ratio,[24] which has been demonstrated in the work performed by Huang et al.[36] They found that the mesoporous silica nanoparticles with an aspect ratio of 4 exhibit much higher cellular uptake than their spherical counterparts. Additionally, the surface patterns of NPs influence cellular internalization. A few studies have addressed the cellular uptake of NPs with irregular surface patterns such as patchy staggered lamellae surface patterns.[31,33,37] For example, Hu et al. found that spherical NPs with a surface pattern of staggered lamellae exhibit faster cellular uptake rate than smooth NPs.[33] Schubertová et al. used computer simulation to investigate the influence of ligand distribution of NPs on uptake efficiency and demonstrated that NPs with homogeneous ligand distributions display the fastest uptake rate.[37] In another study, Verma et al. found that ≈6 nm spherical NPs evenly coated with hydrophobic or anionic ligands offer advantages in cellular internalization over NPs coated with randomly distributed ligands.[38] The above works all revealed the relations between the surface morphologies and the cellular internalization capacities of NPs. However, the investigations about the effect of NPs surface morphologies on the cellular internalization are still limited. And the mechanisms underlying the surface morphology-regulated cellular uptake performance of NPs have not been well understood. Tackling these unresolved issues may benefit the novel design of nanocarriers and even understanding the cellular internalizations of virus particles.

Existing experimental approaches usually suffer from difficulties in capturing detailed information about cellular internalization pathways. Theoretical simulation is a powerful tool that has been successfully applied in studies of cellular internalization pathways.[18,39–44] Performing simulations can provide deep insights into particle–cell interaction behaviors. For example, Shi et al. performed coarse-grained molecular dynamics (CGMD) simulations to study the endocytic behavior of nanotubes.[45] The simulation results revealed the mechanisms underlying the experimental observations. The authors found that the entry angle of nanotubes during endocytosis varies with the density of receptors on the membrane. The solvent-free model adopted in their work is a powerful simulation method because this model maintains the principal properties of cell membrane (e.g., the bending modulus, surface tension, and diffusion constant). Previous works have used this simulation method for understanding the cellular internalization mechanisms of NPs, such as the effect of the NP shape on the endocytic pathways.[42,43] Since experiments can provide straightforward results, whereas simulations provide deep insights into these observations, the combination of experimental and simulation approaches can provide a comprehensive understanding of cellular uptake performance.[27,45]

In this work, a combination of experiments and CGMD simulations was used to investigate the cellular internalization behavior of three types of rod-like NPs, with smooth, abacus-like, and helical-structured surfaces. The NPs were prepared via the cooperative self-assembly of poly(γ-benzyl-L-glutamate)-*b*-poly(ethylene glycol) (PBLG-*b*-PEG) block copolymers and PBLG homopolymers using different initial solvents and temperatures. The CGMD simulations demonstrated how the surface structure regulates the cellular internalization efficiency of NPs. In addition, the simulations revealed novel endocytic pathways for two types of these NPs with stripe-patterned surfaces. The NPs with helical and abacus-like surfaces have "gyroscope-like" (precession) and "standing up" (tip entry) endocytic pathways, respectively, which are distinct from the traditional pathway for NPs with smooth surfaces. These novel endocytic pathways, especially "gyroscope-like" endocytosis, are the main reason for the different cellular uptake performance of these NPs. The simulations reveal the mechanism underlying this difference in uptake, which is difficult to observe via experiments alone. These findings may inspire the synthesis of new NPs for biomedical applications, such as advanced drug delivery systems.

2. Results and Discussion

2.1. Morphology of Aggregates Self-Assembled from the PBLG(FITC)-*b*-PEG/PBLG Binary System

Based on our previous work,[46–48] we prepared rod-like NPs by assembling PBLG(FITC)-*b*-PEG/PBLG mixtures under various initial conditions (the chemical structures of these polymers are given in **Figure 1**a). As revealed by our previous work,[46,48] the self-assembly temperature and the initial solvent play important roles in determining the surface pattern of rod-like NPs. To obtain NPs with various surface patterns, we conducted self-assembly under various temperatures and solvent conditions. First, PBLG(FITC)-*b*-PEG and PBLG were dissolved in a mixed solvent of tetrahydrofuran (THF) and *N,N′*-dimethylformamide (DMF). Water was subsequently added, followed by dialysis to remove the organic solvents. Details of the preparation can be found in Section 1.3 in the Supporting Information.

Via the self-assembly of the PBLG(FITC)-*b*-PEG/PBLG binary system, three types of rod-like NPs with different surface morphologies were obtained. In these nanostructures, PBLG forms a rigid bundle, and PBLG-*b*-PEG wraps around the bundle to form a shell. The packing manner of the block copolymers on the bundle surface can be manipulated by the self-assembly temperature and initial solvent composition, giving rise to different surface patterns.[46] Figure 1b–d shows scanning electron microscope (SEM) images of the three types of rod-like NPs. The insets at the top are transmission electron microscope (TEM) observations, and the insets at the bottom are the simulation-predicted morphologies of these NPs according to our previous work (blue lines denote the PBLG homopolymers, which form the template, while green and red lines denote the PBLG and PEG segments in block copolymers, forming the shells on the template).[46] For the first type of NP, which was prepared with initial solvent THF/DMF = 1/1 by volume at 5 °C, a smooth surface structure can be observed, as shown in Figure 1b. The other two types of NPs have stripe-patterned surfaces. For the NP prepared with initial solvent THF/DMF = 3/7 by volume at 40 °C (see Figure 1c), the stripes are discontinuous, forming abacus-like (beads-on-wire) structures on the rod-like template. Meanwhile, on the third type of NP, the stripes are continuous, and

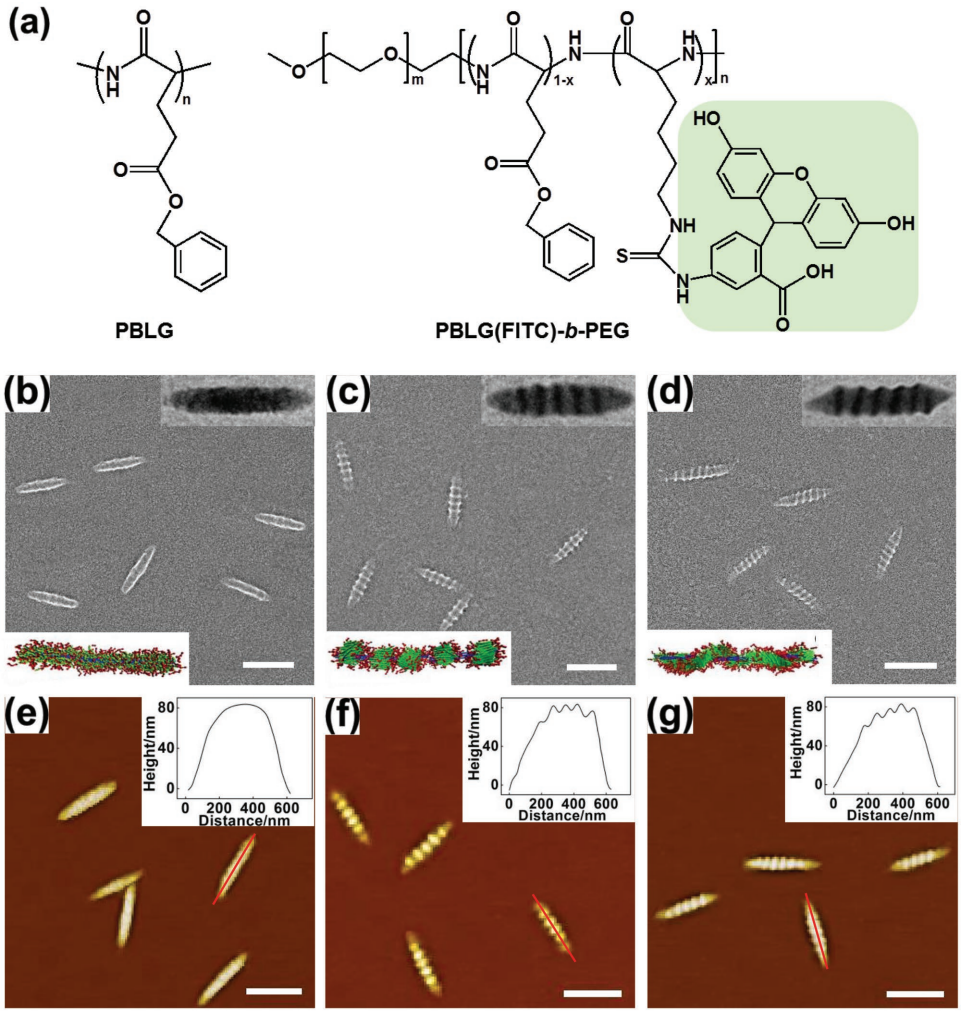

Figure 1. a) Chemical structures of the homopolymer PBLG and the fluorescent-labeled copolymer PBLG(FITC)-*b*-PEG. b–d) SEM and e–g) AFM images of aggregates self-assembled from the PBLG(FITC)-*b*-PEG/PBLG binary systems under different initial conditions. b,e) Smooth NPs, initial solvent THF/DMF = 1/1 by volume at 5 °C; c,f) abacus-like NPs, initial solvent THF/DMF = 3/7 by volume at 40 °C; d,g) helical NPs, initial solvent THF/DMF = 3/7 by volume at 50 °C. Insets at the top of (b), (c), and (d) are corresponding images observed using TEM. Insets at the bottom of (b), (c), and (d) are respective schematic illustrations obtained from simulations in our previous work.[46] Reproduced with permission.[46] Copyright 2013, Wiley-VCH. Insets in (e), (f), (g) are profiles of the three types of surface microstructures measured by AFM along the red lines. Scale bars: 500 nm.

a helical structure is obtained (THF/DMF = 3/7 by volume at 50 °C), as shown in Figure 1d. For simplicity, we have named the three types of NPs smooth, abacus-like, and helical NPs according to their surface microstructures. Figure 1e–g shows atomic force microscopy (AFM) images of these rod-like NPs. The insets are the corresponding profiles of surface patterns measured by AFM. The AFM images and profiles show features on the surface of the smooth, abacus-like, and helical NPs similar to those observed in SEM. The smooth NPs have relatively uniform surfaces (inset in Figure 1e), while the other two types of NPs have regular stripe-patterned surfaces (insets in Figure 1f,g). Detailed structural information on these rod-like NPs is provided in **Table 1**. The sizes of these rod-like NPs are very similar. Measured from the SEM images, the average diameter and length of these rod-like NPs are ≈110 and 610 nm, respectively. We also

Table 1. Detailed structure information for rod-like NPs self-assembled from the PBLG(FITC)-*b*-PEG/PBLG binary system.

NPs	Diameter[a)] [nm]	Length[a)] [nm]	Aspect ratio[a)]	Volume[a)] [10^{-3} μm^3]	$\langle R_h \rangle$[b)] [nm]	PDI[b)]	ξ[c)] [mV]
Smooth	112.3 ± 4.8	625.7 ± 30.3	5.6 ± 0.3	6.2 ± 0.2	125.3	0.208	−2.53 ± 0.5
Abacus-like	113.9 ± 5.2	608.4 ± 26.8	5.3 ± 0.4	6.2 ± 0.2	119.2	0.122	−2.68 ± 0.1
Helical	113.1 ± 6.0	604.8 ± 30.4	5.3 ± 0.2	6.1 ± 0.3	118.5	0.105	−2.29 ± 0.2

[a)]The data were measured from SEM images of the three types of rod-like NPs. The statistical number for each type of NP was 50. Volume values of these NPs were approximated based on the diameter and length of NPs; [b)]Hydrodynamic radii and corresponding polydispersity indices of these NPs were determined by dynamic light scattering measurement at a scattering angle of 90°; [c)]The zeta potentials of the three types of NPs were measured at concentrations of 0.2 g L^{-1} in DMEM.

measured the hydrodynamic radii ($\langle R_h \rangle$) and zeta potentials of these rod-like NPs, in order to characterize them more comprehensively. Methods of the dynamic light scattering (DLS) and zeta potential measurement can be seen in Section 1.7 and 1.8 in the Supporting Information, respectively. The hydrodynamic radii ($\langle R_h \rangle$) of these NPs are ≈120 nm as measured using DLS at a scattering angle of 90°. The corresponding polydispersity indices (PDI) are 0.208, 0.122, and 0.105 for smooth, abacus-like, and helical NPs, respectively. In addition, the mean zeta potentials are –2.53, –2.68, and –2.29 mV for smooth, abacus-like, and helical NPs, respectively, in Dulbecco's modified Eagle's medium (DMEM). The negative zeta potentials are due to the existence of the low level of carboxyl groups in fluorescein isothiocyanate (FITC)-labeled PBLG segments. The three types of NPs have almost the same zeta potentials during the cellular uptake experiment, which means that the effect of the zeta potentials of these NPs on the cellular uptake behavior could be ignored. For details about the characterizations of rod-like NPs (e.g., $\langle R_h \rangle$ and zeta potentials), see Section 2.1 in the Supporting Information.

2.2. Cellular Internalization Behavior of Rod-Like NPs

The cellular internalization of the NPs was examined using NIH3T3 cells. The kinetics of cellular uptake was evaluated by quantifying the results of confocal laser scanning microscopy (CLSM) analysis of a time course from 15 min to 8 h of incubation (**Figure 2**a,b). Because the fluorescent intensities are reduced with increasing temperature in the preparation of samples (samples are prepared at different temperatures), the three types of NPs can exhibit different fluorescent intensities. To rule out this effect, we calibrated the fluorescent intensity of each type of rod-like NP for a quantitative comparison in the following in vitro experiments. Details about the calibration of fluorescent intensity are provided in Section 2.2 in the Supporting Information. As shown in Figure 2a, green fluorescence can be observed at 30 min for all groups, indicating that the three types of NPs were taken up by cells. The green fluorescent intensities increased with time. In addition, at 4 h, the fluorescent intensity was strongest for the helical NP group and weakest for the abacus-like NP group. Figure 2b shows a quantitative characterization of the internalization process. Clearly, the NPs rapidly enter cells during the first 2 h, and this rate then gradually slows down. After ≈6 h of incubation, the fluorescent intensity of the NPs shows no obvious increase with time, indicating that the cellular uptake reaches an equilibrium state. These results show that helical NPs exhibit the most efficient cellular internalization, followed by smooth NPs and abacus-like NPs. Figure 2c shows profiles measured by flow cytometry after 6 h of incubation with the three types of NPs, with IFI representing the average intracellular fluorescent intensity. Compared to that of the control group, the IFI in the other three groups increases, indicating the progress of cellular internalization. In addition, the helical NP group exhibits the highest fluorescent intensity, followed by

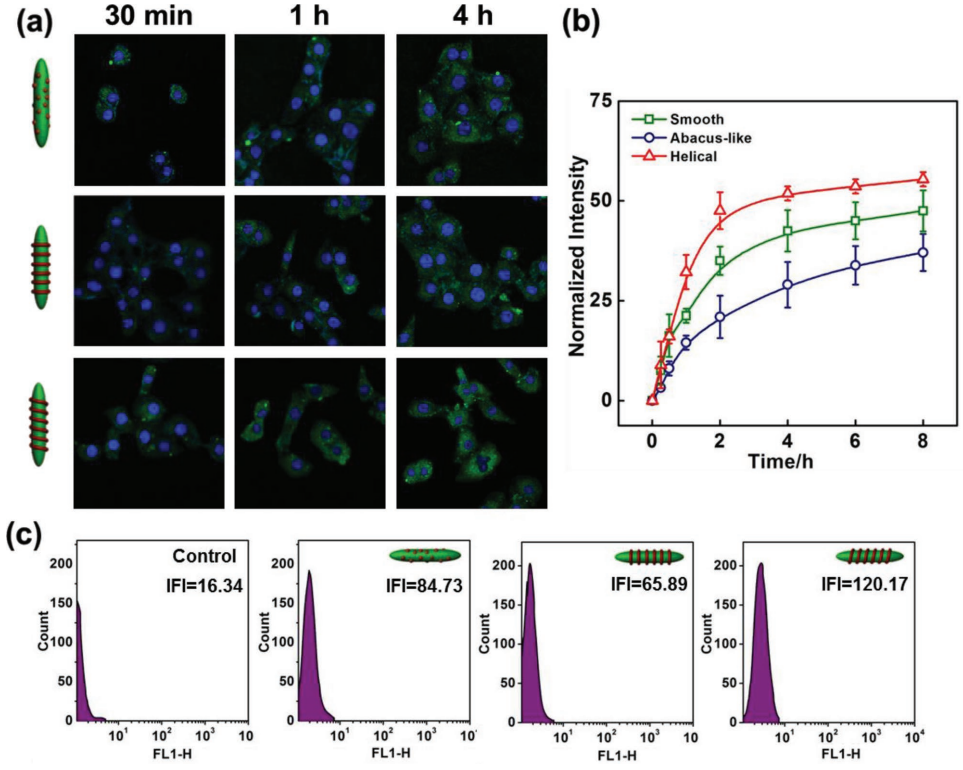

Figure 2. a) Overlay CLSM images of NIH3T3 cells upon incubation with three types of rod-like NPs at varying time intervals. The cell nuclei were stained with DAPI (blue channel), and the green channel fluorescent emission originated from the FITC in the NPs; b) profiles of the normalized fluorescent intensity of the three NPs as a function of time, which were quantified from CLSM observations; c) cellular fluorescence profiles measured by flow cytometry. IFI is the average intracellular fluorescence intensity after incubation with the three nanostructures for 6 h.

the smooth NP group and abacus-like NP group, consistent with the CLSM analysis. Interestingly, these observations demonstrate that the cellular uptake capacity of NPs can be regulated by their surface pattern. Compared to traditional smooth NPs, the helical NPs show superior cellular internalization efficiency, while the abacus-like NPs display decreased uptake.

In addition, detailed information on the NP-internalized cells can be seen in the SEM and CLSM 3D images. The results presented in Figure 2 demonstrate that the cellular internalization of these NPs becomes saturated after 6 h of incubation, which is suitable for SEM observation. The SEM and CLSM observations of NIH3T3 cells incubated with these NPs for 6 h are presented in **Figure 3**. SEM images exhibit information on the membrane surfaces and the CLSM 3D views provide information from inside the cells.[49] Figure 3a exhibits the control group, and Figure 3b–d shows images of a single cell incubated with helical, smooth, and abacus-like NPs in sequence. In the control group, the membrane is relatively flat and smooth, and it exhibits wrinkling in the other three groups (for clear images, see the insets in Figure 3a–d). Figure 3b–d shows bumpy cell morphology and protrusions extending from the cell bodies as a result of the NP uptake. In addition, a small amount of NPs may be enveloped by the cell membrane, which also causes membrane wrinkling.[45,50] Figure 3e is a CLSM 3D overlay image of NIH3T3 cells upon incubation with helical NPs for 6 h, while Figure 3f is the corresponding image from the FITC channel. Green fluorescence appears in the cells, indicating that the helical NPs have entered the cells. Additionally, Figure 3g shows the profile of the fluorescence intensity distribution of a single cell marked in Figure 3e,f. Consistent with the SEM observations, the NPs are mainly concentrated in the cytoplasm, with a few remaining attached to the membrane. The smooth and abacus-like NPs produced similar results (Section 2.3, Supporting Information).

2.3. Investigation of Endocytic Pathways

Generally, NPs on the size scale in the recent reports (50–1000 nm) can enter cells via several pathways, including micropinocytosis, caveolin-dependent endocytosis, and clathrin-dependent endocytosis.[51,52] We further explored the endocytic pathway utilized in the cellular internalization of rod-like NPs. First, we examined the cellular internalization of NPs at two temperatures. At low temperature, the lipid bilayer becomes hardened, thus substantially weakening the endocytic and passive diffusive processes. As a result, cellular internalization via energy-dependent processes decreases.[53] **Figure 4**a shows the cellular uptake capacity upon incubation with the three types of NPs for 2 h at 4 and 37 °C. At the lower temperature, the cellular uptake ability of all three types of NPs is weakened, indicating an energy-dependent process in the cellular internalization.

In order to further understand which of the energy-dependent internalization processes do these NPs follow, we studied the cellular uptake percentage of NPs treated with four types of inhibitors. Figure 4b shows the cellular internalization of the three types of NPs using inhibitors of specific endocytic pathways. NIH3T3 cells were treated with several biochemical inhibitors of energy-dependent processes, caveolae-mediated endocytosis, clathrin-mediated endocytosis, and micropinocytosis before incubation with NPs.[23,33] Compared to the control group with no inhibitors, the groups treated with inhibitors exhibited certain decreases in cellular uptake. In cells treated with NaN_3/2-deoxyglucose (NaN_3/DOG), which is known to inhibit energy-dependent pathways, dramatic decreases in the cellular uptake of all the three types of NPs can be observed (49%–60% decrease compared to the control group). Because some glucose and exogenous ATP remains in the serum-free medium, cellular internalization could not be completely inhibited. In cells treated with methyl-β-cyclodextrin (MβCD), which perturbs the caveolae-mediated endocytosis pathway, cellular uptake

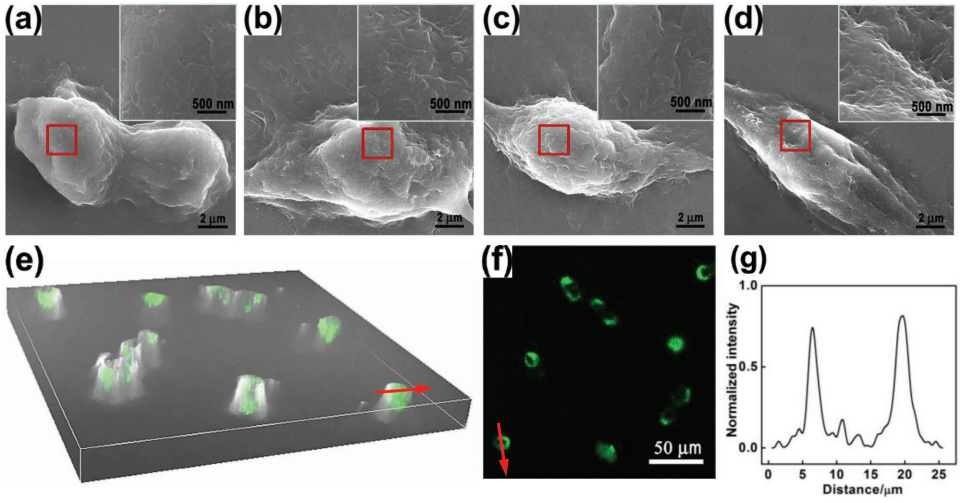

Figure 3. SEM images of NIH3T3 cells incubated with the three rod-like NPs for 6 h: a) control group, b) smooth NPs, c) abacus-like NPs, and d) helical NPs. The insets are enlarged images. CLSM images of NIH3T3 cells upon incubation with helical NPs for 6 h: e) 3D overlay, f) FITC channel, g) fluorescence intensity distribution of the single cell marked in (e) and (f). The red squares in (a–d) illustrate where the images are enlarged. The red arrows in (e) and (f) indicate the direction along which the normalized intensity is calculated (i.e., distance in (g)).

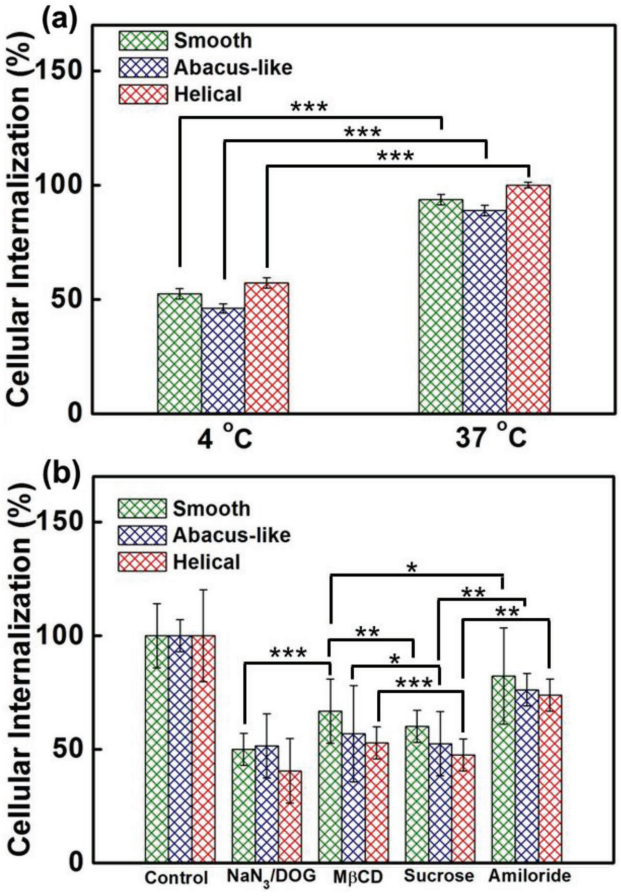

Figure 4. a) Cellular uptake capacity upon incubation with the three types of NPs for 2 h under 4 and 37 °C. b) Cellular internalization of the three types of NPs by using inhibitors of specific endocytic pathways. Percent internalization was normalized to particle internalization in the absence of inhibitors. Data are represented as average ± standard deviation (n = 10). Statistical significance: *p < 0.05, **p < 0.001, ***p < 0.0001.

was somewhat decreased compared to the control group (32%–48%). The cells treated with sucrose, which is used as an inhibitor of clathrin-mediated endocytosis, also showed marked decreases in cellular uptake compared to the control group (42%–52%). Treatment with amiloride, which is employed to block pinocytosis, produced a certain decrease in endocytosis for all three nanostructure types (18%–26% decrease compared to the control group). In addition, p values of these groups were also estimated. The p value is defined as the probability of obtaining a result equal to or "more extreme" than what was actually observed, when the null hypothesis is true. The results can be regarded as statistically significant when $p < 0.05$.[31] The results are shown in Figure 4. As can be seen, the p values of all the contrasted groups are smaller than 0.05. The above results indicate that the differences of these groups are statistically significant.

These observations indicate that the three types of rod-like NPs should enter cells via multiple endocytic pathways. The marked decrease in the cellular internalization percentage for the NaN_3/DOG-treated group demonstrates that the cellular uptake of these NPs is an energy-dependent process. Consequently, all three types of rod-like NPs pass through the cell membrane via energy-dependent endocytic processes, which is consistent with the results obtained at different incubation temperatures (Figure 4a). Since the sucrose group exhibits lowest cellular uptake percentage (45 ± 5%, 50 ± 8%, and 58 ± 6% for the three types of NPs) compared to β-cyclodextrin groups (57 ± 5%, 60 ± 12%, and 71 ± 9%) and amiloride groups (75 ± 5%, 77 ± 6%, and 85 ± 18%), the clathrin-mediated endocytosis should be the most favored endocytosis pathway for these NPs. Similar phenomena have been reported in existing works.[33,45] In addition, the cytotoxicity of these NPs was tested by using the tetrazolium salt assay to ensure the reliability of the quantitative analyses above. No cytotoxicity for NPs was found after 8 h of incubation, indicating good biocompatibility of these rod-like NPs. The methods and detailed results of the cytotoxicity measurement can be found in Sections 1.9 and 2.4 in the Supporting Information, respectively.

2.4. CGMD Simulation of Cellular Internalization

The above experiments reveal that the different endocytic efficiencies in the NPs are regulated by the different surface microstructures. However, experimentally obtaining detailed information about the mechanisms of endocytosis is difficult. To address this challenge, we studied the endocytosis of these NPs by performing CGMD simulations,[45] which is a powerful tool. Our previous studies revealed that PEG segments are highly localized at the screw-thread templates formed by PBLG blocks.[46–48] Details about the packing of PEG can be found in Figure S5 in the Supporting Information. Moreover, the interactions between the distal methoxy groups at the ends of the PEG chains and the membrane surface proteins or lipids have been found to be weaker hydrophobic interactions, or hydrogen bonding, with a binding strength ranging from 2 to 7 k_BT. These methoxy groups at the free ends of PEG polymers essentially act as nonspecific targeting moieties weakly interacting with cell-surface biomolecules.[16] Therefore, these experimentally prepared aggregates can be modeled as rod-like particles (corresponding to the rod-like template) decorated with ligands (corresponding to the PEG segment on the NP surface). The coarse-grained models are shown in **Figure 5**a. The rod-like template is constructed of hydrophobic beads (green), and the ligands (red) are decorated on the rod-like template in three different manners. The plasma membrane is composed of phospholipids. According to the solvent model proposed by Cooke and Deserno, each phospholipid has one hydrophilic head bead and two hydrophobic tail beads, denoted by blue and orange beads, respectively.[54] Some of the phospholipids act as receptors, the head beads of which are colored in purple. Details of the model and simulation method can be found in Section 3.1 in the Supporting Information.

The parameters used in the simulations were set according to those in the experiments. For the NPs in experiments, the aspect ratio (length/diameter) is ≈5.3–5.6. In the simulations, we set the aspect ratio of NPs as 5.5. The diameter and length of the rod-like particles are 8 and 44σ (σ denotes a length unit), respectively. Since the free end of PEG segments

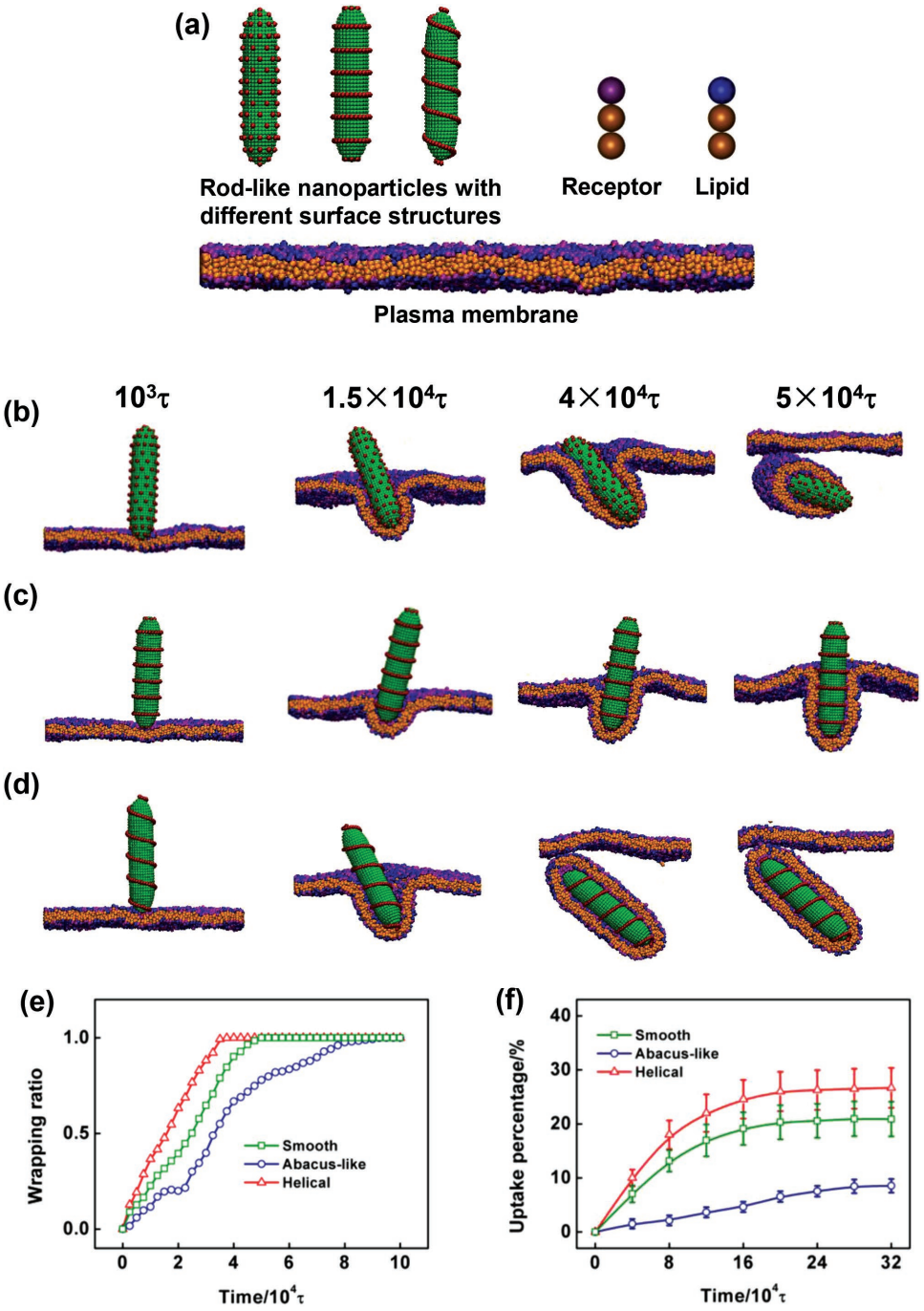

Figure 5. a) Coarse-grained models in the simulation. Snapshots during the endocytosis of these NPs with different surface microstructures: b) smooth; c) abacus-like; and d) helical. e) Wrapping percentage of a single NP as a function of time. f) Uptake percentage as a function of time.

(acting as ligands) can bind to the proteins in a membrane (acting as receptors) with a strength of 2–7 k_BT,[16] we set the receptor–ligand binding strength to $5\varepsilon_0$ ($1\varepsilon_0 = 1\ k_BT$) in the simulations. The surface tension of the plasma membrane was kept at zero during the simulations. For details about the parameter setting and simulation system in the simulations, see Sections 3.2 and 3.3 in the Supporting Information, respectively.

The experiments in the present work reveal that the major cellular uptake pathway is clathrin-mediated endocytosis, which is energy dependent (Figure 4). In the CGMD simulations, the interaction pathway between the NPs and the membrane is also receptor-mediated endocytosis, which can mimic the experimental situations well. Figure 5b–d shows the endocytic pathways of single NP. Helical NPs have the best endocytic efficacy, followed by smooth NPs and abacus-like NPs. The evolutionary wrapping ratios (denoted by η) as a function of time also demonstrate this phenomenon, as shown in Figure 5e. The helical and abacus-like NPs exhibit the fastest and slowest increases in η, respectively, indicating the predominant endocytic efficiency of helical NPs. We additionally performed simulations to study the cellular

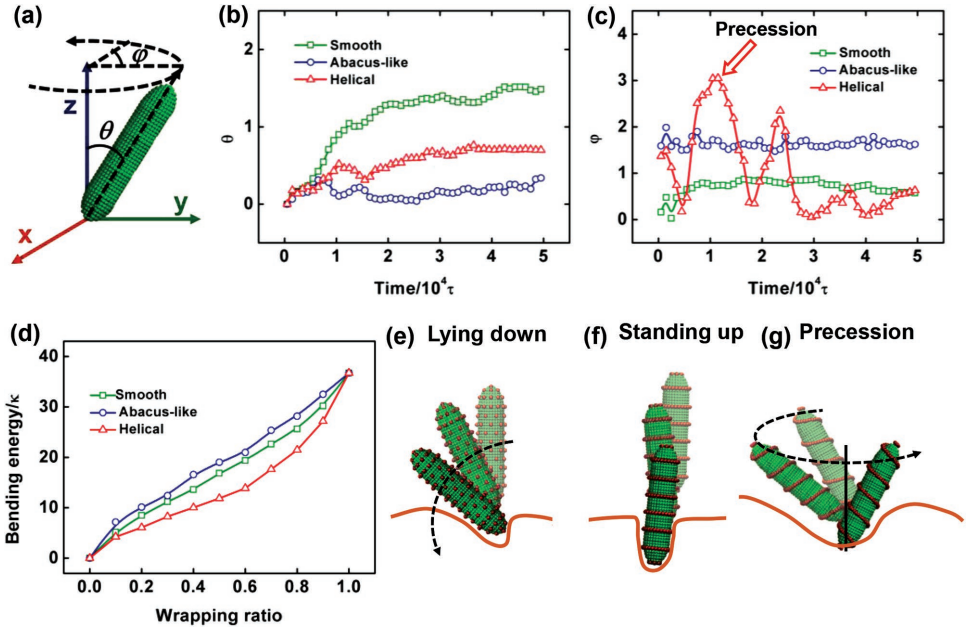

Figure 6. a) Schematic of the angle. b,c) Evolution of the angle of the three NPs as a function of time. d) Bending energy of a plasma membrane as a function of the wrapping ratio during the endocytosis of rod-like NPs. e–g) Mechanism for the different bending energies of NPs.

uptake percentage of each type of NP as a function of time, by performing the simulations 20 times with various initial distances between the NPs and membrane. The statistical results are shown in Figure 5f. The results are qualitatively consistent with the experimental ones shown in Figure 2b, indicating that the internalization capacity of the NPs follows the sequence helical > smooth > abacus-like NPs. These theoretical predictions firmly validate the experiments, although the quantitative match is difficult to obtain due to the limitations of current computation abilities.[18,45,47]

2.5. Novel Endocytosis Pathways for Helical and Abacus-Like NPs

After carefully examining the endocytic processes of these NPs, novel entry pathways were identified for helical and abacus-like NPs. We calculated the entry angle, θ (the angle between the major axis of the NP and the normal direction of the membrane), and the precession angle, φ (the rotation angle of the major axis of the NP about the normal direction of the membrane). The definitions of the two angles are shown schematically in **Figure 6**a. The evolution of θ and φ as a function of time for the three types of NPs is presented in Figure 6b,c. The highest and lowest θ values during endocytosis were observed for the smooth and abacus-like NPs, respectively. The extremely small contact angle of the abacus-like NP indicates a "standing up" ($\theta \approx 0$, i.e., tip entry) endocytic pathway. Noted that helical NPs show a cosine/sine wave in φ angle profile, as shown in Figure 6c; this phenomenon corresponds to a "gyroscope-like" entry (wherein the major axis of the NP rotates about the normal direction of the membrane, i.e., precession). Movies of the endocytosis for the three NPs are provided in the Supporting Information. The "standing up" and "gyroscope-like" endocytic pathways for the abacus-like and helical NPs are almost independent of the initial contact angle (θ_0) between the NPs and membrane. Simulation results for the three types of NPs under other θ_0 ($\pi/6$ and $\pi/3$) can be found in Section 3.4 in the Supporting Information.

The unique endocytic pathways for the novel NPs with stripe-patterned surfaces may be responsible for the different cellular uptake capacities of these NPs. While being endocytosed, the NPs must overcome the bending energy (E_b) of the membrane.[42,43] The formula for E_b is provided in Section 3.1 in the Supporting Information. Figure 6d shows the profiles of E_b/κ, where κ denotes the bending modulus of the membrane, as a function of the wrapping ratio for the three types of NPs. The increase in E_b/κ for helical NPs is slower than those for smooth and abacus-like NPs, which indicates a lower energy barrier for the helical NPs to complete endocytosis. Consequently, the helical NPs have greater endocytic capability. According to the formula of E_b, the bending energy is associated with the membrane curvature. Lower E_b corresponds to less curvature during endocytosis, which is favorable for the completion of endocytosis. The schematics of the endocytic pathways for the three types of NPs are illustrated in Figure 6e–g. For abacus-like NPs, "standing up" endocytosis without rotation leads to a large principal curvature of the membrane. The traditional "lying down" of smooth NPs may reduce the curvature of the membrane. Interestingly, due to precession, in which the main axis of the NP rotates around the normal direction of the membrane, helical NPs produce the smallest membrane curvature during endocytosis.

2.6. Potential Applications of NPs with Various Surface Patterns

Generally, in the existing works regarding the cellular internalization of NPs, most of the NPs usually follow the

traditional endocytosis pathways. In addition, the mechanisms underlying the relations between the surface morphologies of NPs and the cellular uptake capacity have not been well understood. Our experiment-simulation combined investigation on the cellular internalization of NPs with stripe-patterned surfaces addresses above challenges and contributes in several unprecedented discoveries. We found that, by introducing helically distributed ligands onto the surface of rod-like NPs, a "gyroscope-like" entry occurs, which has not been observed or predicted before. Our theoretical analysis shows that this novel endocytosis pathway could lead to a different internalization capacity of NPs. In addition, the present work proposed a new approach to control the cellular internalization capacity of NPs: regulating their surface pattern. Previous investigations have proven that desirable cellular uptake of NPs can be achieved by tuning various factors, such as the size, shape, and ligand density.[18,39–43] However, these factors may be difficult to control in some circumstances. For example, it could be quite difficult to increase the ligand density because of the limited free space on the surface of NPs. Consequently, the cellular internalization performance may be poor when NPs have a relatively low ligand density. Our investigations show that by introducing helical structures onto the surface of NPs (i.e., with the ligands showing a helical distribution), a greater cellular uptake capacity could be achieved. In contrast, sometimes a weaker endocytic efficacy is desirable because faster cellular uptake of rigid NPs could lead to higher cytotoxicity.[39] In this case, the NPs with abacus-like surface structures may be a good choice for reducing cellular uptake efficiency. This simple approach to producing tunable cellular internalization performance may be helpful for various applications of novel biomaterials, especially when utilized as an advanced drug delivery system. In addition, this study can be beneficial for developing potential bio-mimicking applications of polymeric self-assembly, for example, imitating the nature of virus-like NPs. Striped patterns can be found on the capsids of virus particles (including those of Poxviridae). These surface structures are thought to play important roles in the activities of virus particles during their lifetimes. The present work revealed the different endocytic pathways and capacities of the virus-like NPs with various surface structures. Our research demonstrates a practical way to prepare virus-like NPs, which may function as novel particles for biorelated applications.

3. Conclusion

In summary, we examined the cellular internalization of rod-like NPs with three types of surface microstructures, i.e., smooth, abacus-like (beads-on-wires) and helical, which were prepared by the cooperative self-assembly of PBLG(FITC)-*b*-PEG and PBLG. The in vitro experimental results show that all three NPs can be internalized, mainly via endocytosis. Helical NPs exhibit the best endocytic efficacy, followed by smooth NPs and abacus-like NPs. The coarse-grained molecular dynamic simulations reproduced these variations in the endocytic performance. Impressively, helical NPs can enter the plasma membrane via a unique "gyroscope-like" (precession) pathway, and abacus-like NPs exhibit a "standing up" (tip entry) pathway. This phenomenon is responsible for the distinct cellular uptake efficiencies of these NPs because of the increased or decreased membrane curvature during the endocytosis of abacus-like or helical NPs, respectively. The cellular internalization capacity can be regulated by introducing a stripe pattern (abacus-like or helical) to the surface of rod-like NPs. This study may be beneficial for biomaterial applications in several fields, such as advanced drug delivery systems.

4. Experimental Section

Materials: Methoxypolyethylene glycol amine (M_w = 5000) was purchased from Sigma-Aldrich Inc. (USA). *N'*-FMOC-l-lysine was purchased from GL Biochem Ltd. (Shanghai, China). FITC was purchased from Adamas-beta Inc (Shanghai, China). The PBLG homopolymer and the PBLG(FITC)-*b*-PEG copolymer were synthesized according to previous reports.[55–57] Details about the synthesis and characterization are provided in Sections 1.1 and 1.2 in the Supporting Information.

Preparation of Rod-Like NPs: Rod-like aggregates were prepared via the dialysis method according to the previous work.[46,48] For the smooth NPs, PBLG(FITC)-*b*-PEG and PBLG were dissolved in THF/DMF mixture (1:1, v:v), and the aggregate solution was prepared at 5 °C. For the abacus-like NPs, PBLG(FITC)-*b*-PEG and PBLG were dissolved in THF/DMF mixture (3:7, v:v), and the aggregate solution was prepared at 40 °C. For the helical NPs, PBLG(FITC)-*b*-PEG and PBLG were dissolved in THF/DMF mixture (3:7, v:v), and the aggregate solution was prepared at 50 °C. Details about the experimental information are available in Section 1.3 in the Supporting Information. All experimental procedures, including the processes of adding water and dialysis, were performed at the corresponding temperature. The polymer solutions and water were stored at the corresponding temperature for more than 12 h before use. All preparation processes were shielded from light. Before further experiments, the solutions were stabilized for at least 5 d. The aggregate morphology was characterized by TEM (JEM-2100F, 200 kV), SEM (S4800, 15 kV), and AFM (XE-100, noncontact mode). Details about the testing method can be found in Sections 1.4–1.6 in the Supporting Information.

Cellular Uptake of FITC-Labeled Rod-Like NPs: The cellular uptake of the NPs was conducted on model cells of NIH3T3. The cells were seeded in 24 well plates at 5×10^4 cells per well in 1 mL of DMEM containing 10% fetal bovine serum, 100 μg mL^{-1} penicillin, and 100 μg mL^{-1} streptomycin, and cultured at 37 °C in a humidified atmosphere of 5% CO_2 for 24 h, followed by removing the culture medium and adding DMEM containing the aggregates. The cells were incubated with aggregates for a series of time intervals from 15 min to 2 h. After a total of 8 h of incubation, the aggregate solution was removed, and the cells were rinsed three times with PBS and fixed with 4% formaldehyde for 15 min at 4 °C The cell nuclei were stained with 4′,6-diamidino-2-phenylindole (DAPI, blue). The cells were analyzed with a confocal laser scanning microscope (A1R, Nikon). Ten images of each type of rod-like NPs were used for quantitative characterization of the fluorescent intensity. The results were obtained as the mean and standard deviation based on these images. To ensure the accuracy of the

CLSM test, the authors performed all the measurements under the same conditions, as follows: 600× magnification, refraction index of 1.51, and numerical aperture of 1.40. The emission and excitation wavelengths for FITC were set to 525.0 and 488.0 nm, respectively.

Inhibition Studies of Endocytosis: The studies of endocytosis inhibition were performed as follows. NIH3T3 cells were seeded in 24 well plates at 5×10^4 cells per well in 1 mL of DMEM and cultured at 37 °C in a humidified atmosphere of 5% CO_2 for 24 h. The cells were separately treated with 0.1% NaN_3/50×10^{-3} M 2-deoxyglucose for 1 h, 5×10^{-3} M MβCD for 15 min, 225×10^{-3} M sucrose for 30 min or 1×10^{-3} M amiloride for 30 min. Each medium was then replaced fresh medium containing the corresponding inhibitor plus the rod-like NPs and further incubated at 37 °C in a humidified atmosphere of 5% CO_2 for 2 h. Then, the media were removed, and the cells were rinsed three times with PBS and fixed with 4% formaldehyde for 15 min at 4 °C. The cell nuclei were stained with DAPI. Cells were analyzed with CLSM.

CGMD Simulation Method: The solvent-free method, proposed by Cooke and Deserno,[54] was adopted in the simulations in the present work. This method maintains the principal properties of the cell membrane. Because there are no solvent beads in the method, the simulation can be performed efficiently, and greater time and size simulation scales can be realized. This method has been successfully applied to study the endocytosis of NPs.[42,45]

In this method, the bonds linking two neighbored beads in lipids or receptors are defined by a finite extensible nonlinear elastic potential:

$$U_{\text{bond}}(r) = -1/2k_b r_b^2 \ln\left[1-(r/r_b)^2\right] \quad (1)$$

where k_b and r_b are the strength of the potential and the maximum extent of the bond, respectively. Additionally, a harmonic spring potential is applied between the head and second tail beads to maintain a straightened shape in the lipids:

$$U_{\text{angle}}(r) = 1/2k_a(r-r_a)^2 \quad (2)$$

in which k_a and r_a are the strength of the potential and the equilibrium bond distance, respectively.

In this model, the potentials between all the beads are represented as follows:

$$U_{\text{inter}}(r) = \begin{cases} 4\varepsilon_0\left[(\lambda\sigma/r)^{12} - (\lambda\sigma/r)^6\right], & r < r_{\text{cut}} \\ -\varepsilon_{\text{atr}}\cos^2\left[\pi(r-r_{\text{cut}})/2r_{\text{atr}}\right], & r_{\text{cut}} \le r \le r_{\text{cut}} + r_{\text{atr}} \\ 0, & r > r_{\text{cut}} + r_{\text{atr}} \end{cases} \quad (3)$$

The top piece of the function is a Lennard–Jones potential. ε_0 is the interaction strength and is set as the energy unit in the present work. σ and λ are the length unit and modulus, respectively. r_{cut} denotes the cut-off distance of the first potential. The middle piece of the function represents the attraction between all tail beads of lipids, and the binding between ligands and receptors. ε_{atr} and $r_{\text{cut}} + r_{\text{atr}}$ are the interaction strength and cut-off distance of the second potential, respectively.

The simulations were performed under $N\Sigma T$ ensemble (N, Σ, and T denote the number of beads, membrane lateral tension, and system temperature, respectively). A Langevin thermostat, as developed by Grest and Kremer, was used to maintain constant temperature in the present simulations.[58] In addition, the authors adopted a constant lateral tension condition for the plasma membrane in the simulations. Here, a modified Berendsen barostat was used to maintain the desired lateral tension.[59] Details regarding the simulation model and parameter setting can be found in Sections 3.1 and 3.2 in the Supporting Information, respectively.

The simulation box is $70 \times 70 \times 200\ \sigma$ in size. The CGMD simulations were run for at least 5×10^6 dt, where the time step dt was set to 0.01 τ (τ is the time unit). The initial distance between the center of the nanoparticles and membrane (d_{NM}) was set to 16 σ, and the major axis of the nanoparticle was vertical to the membrane. In the investigation of the cellular uptake percentage as a function of time, the authors performed the simulations 20 times for each nanoparticle under various d_{NM}, which ranged from 16 to 36 σ, and each nanoparticle was given an initial velocity of $-5\ \sigma/\tau$ in the z direction toward the membrane.

Supporting Information

Supporting Information is available from the Wiley Online Library or from the author.

Acknowledgements

J.X. and Z.G. contributed equally to this work. This work was supported by the National Natural Science Foundation of China (21234002, 21474029, 51303055, and 51573049) and the National Key Research and Development Program of China (2016YFC1102900). Support from Project of Shanghai Municipality (15QA1401400, 15ZZ028, and 14DZ2261205) is also appreciated.

Conflict of Interest

The authors declare no conflict of interest.

[1] S. Mura, J. Nicolas, P. Couvreur, *Nat. Mater.* **2013**, *12*, 991.
[2] D. Kakkar, S. Mazzaferro, J. Thevenot, C. Schatz, A. Bhatt, B. S. Dwarakanath, H. Singh, A. K. Mishra, S. Lecommandoux, *Macromol. Biosci.* **2015**, *15*, 124.
[3] Y. Wang, Y. Wang, J. Xiang, K. Yao, *Biomacromolecules* **2010**, *11*, 3531.
[4] X. Yang, J. J. Grailer, I. J. Rowland, A. Javadi, S. A. Hurley, V. Z. Matson, D. A. Steeber, S. Gong, *ACS Nano* **2010**, *4*, 6805.
[5] N. Lee, H. R. Cho, M. H. Oh, S. H. Lee, K. Kim, B. H. Kim, K. Shin, T.-Y. Ahn, J. W. Choi, Y.-W. Kim, S. H. Choi, T. Hyeon, *J. Am. Chem. Soc.* **2012**, *134*, 10309.
[6] S. B. Hartono, W. Gu, F. Kleitz, J. Liu, L. He, A. P. J. Middelberg, C. Yu, G. Lu, S. Qiao, *ACS Nano* **2012**, *6*, 2104.
[7] Y. Shan, T. Luo, C. Peng, R. Sheng, A. Cao, X. Cao, M. Shen, R. Guo, H. Tomás, X. Shi, *Biomaterials* **2012**, *33*, 3025.

[8] E. Haladjova, S. Rangelov, C. B. Tsvetanov, V. Posheva, E. Peycheva, V. Maximova, D. Momekova, G. Mountrichas, S. Pispas, A. Bakandritsos, *Langmuir* **2014**, *30*, 8193.
[9] C. Cai, J. Lin, Y. Lu, Q. Zhang, L. Wang, *Chem. Soc. Rev.* **2016**, *45*, 5985.
[10] X. Zhu, L. Wang, J. Lin, L. Zhang, *ACS Nano* **2010**, *4*, 4979.
[11] T. Jiang, L. Wang, S. Lin, J. Lin, Y. Li, *Langmuir* **2011**, *27*, 6440.
[12] Z. Xu, J. Lin, Q. Zhang, L. Wang, X. Tian, *Polym. Chem.* **2016**, *7*, 3783.
[13] L. Chen, T. Jiang, C. Cai, L. Wang, J. Lin, X. Cao, *Adv. Healthcare Mater.* **2014**, *3*, 1508.
[14] S. Hua, Y. Li, Y. Liu, W. Xiao, C. Li, F. Huang, X. Zhang, R. Zhuo, *Macromol. Rapid Commun.* **2010**, *31*, 81.
[15] B. Pelaz, P. del Pino, P. Maffre, R. Hartmann, M. Gallego, S. Rivera-Fernandez, J. M. de la Fuente, G. U. Nienhaus, W. J. Parak, *ACS Nano* **2015**, *9*, 6996.
[16] C. D. Walkey, J. B. Olsen, H. Guo, A. Emili, W. C. W. Chan, *J. Am. Chem. Soc.* **2012**, *134*, 2139.
[17] L. D. Unsworth, H. Sheardown, J. L. Brash, *Langmuir* **2008**, *24*, 1924.
[18] Y. Li, M. Kroger, W. K. Liu, *Biomaterials* **2014**, *35*, 8467.
[19] A. E. Nel, L. Madler, D. Velegol, T. Xia, E. M. V. Hoek, P. Somasundaran, F. Klaessig, V. Castranova, M. Thompson, *Nat. Mater.* **2009**, *8*, 543.
[20] J. Deng, C. Gao, *Nanotechnology* **2016**, *27*, 412002.
[21] Q. Gan, D. Dai, Y. Yuan, J. Qian, S. Sha, J. Shi, C. Liu, *Biomed. Microdevices* **2012**, *14*, 259.
[22] S. Zhang, J. Li, G. Lykotrafitis, G. Bao, S. Suresh, *Adv. Mater.* **2009**, *21*, 419.
[23] S. E. Gratton, P. A. Ropp, P. D. Pohlhaus, J. C. Luft, V. J. Madden, M. E. Napier, J. M. DeSimone, *Proc. Natl. Acad. Sci. USA* **2008**, *105*, 11613.
[24] H. Meng, S. Yang, Z. Li, T. Xia, J. Chen, Z. Ji, H. Zhang, X. Wang, S. Lin, C. Huang, H. Zhou, J. I. Zink, A. E. Nel, *ACS Nano* **2011**, *5*, 4434.
[25] O. Shimoni, Y. Yan, Y. Wang, F. Caruso, *ACS Nano* **2013**, *7*, 522.
[26] Y. Geng, P. Dalhaimer, S. Cai, R. Tsai, M. Tewari, T. Minko, D. E. Discher, *Nat. Nanotechnol.* **2007**, *2*, 249.
[27] J. Sun, L. Zhang, J. Wang, Q. Feng, D. Liu, Q. Yin, D. Xu, Y. Wei, B. Ding, X. Shi, X. Jiang, *Adv. Mater.* **2015**, *27*, 1402.
[28] W. Liu, X. Zhou, Z. Mao, D. Yu, B. Wang, C. Gao, *Soft Matter* **2012**, *8*, 9235.
[29] Z. Ge, S. Liu, *Chem. Soc. Rev.* **2013**, *42*, 7289.
[30] X. Yang, J. J. Grailer, S. Pilla, D. A. Steeber, S. Gong, *Bioconjugate Chem.* **2010**, *21*, 496.
[31] Y. Niu, M. Yu, S. B. Hartono, J. Yang, H. Xu, H. Zhang, J. Zhang, J. Zou, A. Dexter, W. Gu, C. Yu, *Adv. Mater.* **2013**, *25*, 6233.
[32] X. Xu, H. Yuan, J. Chang, B. He, Z. Gu, *Angew. Chem. Int. Ed.* **2012**, *51*, 3130.
[33] X. Hu, J. Hu, J. Tian, Z. Ge, G. Zhang, K. Luo, S. Liu, *J. Am. Chem. Soc.* **2013**, *135*, 17617.
[34] S. Venkataraman, J. L. Hedrick, Z. Y. Ong, C. Yang, P. L. R. Ee, P. T. Hammond, Y. Y. Yang, *Adv. Drug Delivery Rev.* **2011**, *63*, 1228.
[35] J. A. Champion, S. Mitragotri, *Proc. Natl. Acad. Sci. USA* **2006**, *103*, 4930.
[36] X. Huang, X. Teng, D. Chen, F. Tang, J. He, *Biomaterials* **2010**, *31*, 438.
[37] V. Schubertová, F. J. Martinez-Veracoechea, R. Vacha, *Soft Matter* **2015**, *11*, 2726.
[38] A. Verma, O. Uzun, Y. Hu, Y. Hu, H. S. Han, N. Watson, S. Chen, D. J. Irvine, F. Stellacci, *Nat. Mater.* **2008**, *7*, 588.
[39] K. Yang, Y. Ma, *Nat. Nanotechnol.* **2010**, *5*, 579.
[40] Y. Li, X. Li, Z. Li, H. Gao, *Nanoscale* **2012**, *4*, 3768.
[41] H. Ding, Y. Ma, *Small* **2015**, *11*, 1055.
[42] R. Vácha, F. J. Martinez-Veracoechea, D. Frenkel, *Nano Lett.* **2011**, *11*, 5391.
[43] C. Huang, Y. Zhang, H. Yuan, H. Gao, S. Zhang, *Nano Lett.* **2013**, *13*, 4546.
[44] J. Liang, P. Chen, B. Dong, Z. Huang, K. Zhao, L.-T. Yan, *Biomacromolecules* **2016**, *17*, 1834.
[45] X. Shi, A. von dem Bussche, R. H. Hurt, A. B. Kane, H. Gao, *Nat. Nanotechnol.* **2011**, *6*, 714.
[46] C. Cai, Y. Li, J. Lin, L. Wang, S. Lin, X.-S. Wang, T. Jiang, *Angew. Chem. Int. Ed.* **2013**, *52*, 7732.
[47] Y. Li, T. Jiang, S. Lin, J. Lin, C. Cai, X. Zhu, *Sci. Rep.* **2015**, *5*, 10137.
[48] C. Cai, J. Lin, X. Zhu, S. Gong, X.-S. Wang, L. Wang, *Macromolecules* **2016**, *49*, 15.
[49] B. He, L. Yuan, W. Dai, W. Gao, H. Zhang, X. Wang, W. Fang, Q. Zhang, *Nanoscale* **2016**, *8*, 6129.
[50] C. W. Evans, M. Fitzgerald, T. D. Clemons, M. J. House, B. S. Padman, J. A. Shaw, M. Saunders, A. R. Harvey, B. Zdyrko, I. Luzinov, G. A. Silva, S. A. Dunlop, K. S. Iyer, *ACS Nano* **2011**, *5*, 8640.
[51] S. D. Conner, S. L. Schmid, *Nature* **2003**, *422*, 37.
[52] S. Zhang, H. Gao, G. Bao, *ACS Nano* **2015**, *9*, 8655.
[53] C. Liu, X. Zhen, X. Wang, W. Wu, X. Jiang, *Soft Matter* **2011**, *7*, 11526.
[54] I. R. Cooke, M. Deserno, *J. Chem. Phys.* **2005**, *123*, 224710.
[55] C. Cai, L. Wang, J. Lin, X. Zhang, *Langmuir* **2012**, *28*, 4515.
[56] G. J. M. Habraken, M. Peeters, C. H. J. T. Dietz, C. E. Koning, A. Heise, *Polym. Chem.* **2010**, *1*, 514.
[57] Z. Zhuang, X. Zhu, C. Cai, J. Lin, L. Wang, *J. Phys. Chem. B* **2012**, *116*, 10125.
[58] G. S. Grest, K. Kremer, *Phys. Rev. A: At., Mol., Opt. Phys.* **1986**, *33*, 3628.
[59] H. J. C. Berendsen, J. P. M. Postma, W. F. van Gunsteren, A. DiNola, J. R. Haak, *J. Chem. Phys.* **1984**, *81*, 3684.

Received: December 21, 2016
Revised: March 17, 2017
Published online: May 2, 2017